6th WMO Data Assimilation Symposium

SPECIAL
COLLECTION

Comparison of the Impacts of Momentum Control Variables on High-Resolution Variational Data Assimilation and Precipitation Forecasting

JUANZHEN SUN AND HONGLI WANG

National Center for Atmospheric Research,* Boulder, Colorado

WENXUE TONG

Nanjing University of Information Science and Technology, Nanjing, China

YING ZHANG

National Center for Atmospheric Research,* Boulder, Colorado

CHUNG-YI LIN

Taiwan Typhoon and Flood Research Institute, Taipei, Taiwan

DONGMEI XU

Nanjing University of Information Science and Technology, Nanjing, China

(Manuscript received 20 June 2014, in final form 25 September 2015)

ABSTRACT

The momentum variables of streamfunction and velocity potential are used as control variables in a number of operational variational data assimilation systems. However, in this study it is shown that, for limited-area high-resolution data assimilation, the momentum control variables ψ and χ ($\psi\chi$) pose potential difficulties in background error modeling and, hence, may result in degraded analysis and forecast when compared with the direct use of x and y components of wind (UV). In this study, the characteristics of the modeled background error statistics, derived from an ensemble generated from Weather Research and Forecasting (WRF) Model real-time forecasts of two summer months, are first compared between the two control variable options. Assimilation and forecast experiments are then conducted with both options for seven convective events in a domain that encompasses the Rocky Mountain Front Range using the three-dimensional variational data assimilation (3DVar) system of the WRF Model. The impacts of the two control variable options are compared in terms of their skills in short-term qualitative precipitation forecasts. Further analysis is performed for one case to examine the impacts when radar observations are included in the 3DVar assimilation. The main findings are as follows: 1) the background error modeling used in WRF 3DVar with the control variables $\psi\chi$ increases the length scale and decreases the variance for u and v, which causes negative impact on the analysis of the velocity field and on precipitation prediction; 2) the UV-based 3DVar allows closer fits to radar wind observations; and 3) the use of UV control variables improves the 0–12-h precipitation prediction.

1. Introduction

The variational data assimilation (DA) technique has been widely used in operational centers as well as in research communities to provide analysis and initialization for numerical models. The technique can be implemented with a three-dimensional (3DVar) or a four-dimensional (4DVar) variational data assimilation

approach; the latter requires the use of a prediction model as the constraint. The variational method seeks to find the optimal analysis by minimizing a cost function that measures the discrepancies of the atmospheric state from a background (i.e., a model forecast) as well as from observations. The control variables can be the prognostic model variables or any diagnostic variables derived from them. Three pairs of control variables for momentum are typically used in variational DA systems: streamfunction and velocity potential ($\psi\chi$), eastward and northward velocity components (UV), and vorticity and divergence ($\zeta\delta$). Historically, the $\psi\chi$ and $\zeta\delta$ momentum pairs have been used as control variables in global DA systems and in some regional DA systems that primarily assimilate large-scale observations (Derber and Bouttier 1999; Lorenc et al. 2000; Berre 2000; Ingleby 2001; Zupanski et al. 2005; Rawlins et al. 2007; Huang et al. 2009; Barker et al. 2004, 2012; Wang et al. 2013a,b; Xiao et al. 2005). In contrast, the UV control variables have been the choice for variational systems that emphasize mesoscale data assimilation using observations that have higher densities (Zou et al. 1995; Sun et al. 1991; Sun and Crook 1997; Gao et al. 1999).

Wu and Purser (2002) pointed out that an advantage in using $\psi\chi$ is that the relation between the mass field and the streamfunction is linear under the geostrophic assumption so that statistical regression between the two is possible. The balance between the mass and wind fields is important because it can project information from one variable to the others and minimize initial balance adjustment and spinup when a forecast is launched. The balance part of the streamfunction with each of the other variables can then be subtracted, resulting in a set of control variables that includes streamfunction, unbalanced velocity potential, unbalanced temperature, unbalanced surface pressure, and humidity.

Xie and MacDonald (2012) performed mathematical analysis on cost function formulations with different momentum control variables in the context of limited-area DA and showed that a $\psi\chi$ variational system tends to produce analyses that possess large-scale motions of the background field. It has the tendency to ignore the small-scale information of observation networks and instead to treat it as an uncertainty unless a perfect error covariance is known. In comparison, a UV system can combine the background and observations for smaller scales. They also found that a $\psi\chi$ system possesses a property of preserving the integral value of wind due to the fact that $\psi\chi$ are essentially the integration of UV, which can potentially introduce nonphysical errors to its analysis increment fields. In addition, they pointed out

that another difficulty in using $\psi\chi$ as control variables on a limited-area domain arises from the treatment of lateral boundary conditions in solving the Poisson equations to convert between $\psi\chi$ and the forecast variables UV.

The study by Xie and MacDonald (2012) raises the question whether using $\psi\chi$ as the control momentum variables is still beneficial when an increasing number of high-resolution observations is being used in limited-area convection-permitting data assimilation systems. In these systems, the main goal is to analyze atmospheric flow at the convective scale for improved short-term prediction of high-impact weather. As such, the large-scale balance (such as geostrophic) is no longer dominant for the small spatial and short time scales of interest, and therefore the benefit of using diagnosed momentum variables such as $\psi\chi$ might disappear. Berre (2000) showed that the percentage of the variance of surface pressure that can be explained by balanced geopotential drops quickly with horizontal scale for a limited-area mesoscale model. Since there is no easily defined balance that can be used for the small scale, the primary concern for data assimilation at the convection-permitting scale using a limited-area model is to extract small-scale information from high-resolution observations. Therefore, early data assimilation studies with the primary goal to obtain convective-scale analyses used UV as control variables, out of belief that their direct links to the observations would allow more accurate extraction of small-scale information from the observations. As major NWP systems are moving toward the capability of resolving both large-scale and small-scale flows, it is timely to compare the impact of the choice of momentum control variables on high-resolution analysis. In the current study, we only focus on the two pairs of control variables, $\psi\chi$ and UV. Although the study by Xie and MacDonald (2012) laid the groundwork for understanding the behaviors of the two pairs of control variables, they have not been compared with real observations in terms of convective forecasting.

In this paper, we present results from real-data experiments that compare the two pairs of momentum control variables, $\psi\chi$ and UV, in the context of high-resolution analysis aimed at improved short-term convective forecasting. Our experiments are conducted using the 3DVar system developed for the Advanced Research version of the Weather Research and Forecasting (WRF) Model (WRFVAR) (Barker et al. 2004, 2012). One issue that is not investigated by Xie and MacDonald (2012) but can impact the quality of the analysis and forecast is the different background error (BE) statistics of velocity resulting from the use of different momentum control variables. This issue is

examined in the current study by comparing the BE statistics of the two control variable options derived from two months of warm season WRF forecasts. We then use these error statistics in real-data 3DVar experiments of seven cases to examine their impacts on convective forecasting. The 3DVar DA experiments for the multiple cases were performed with continuous update cycles with conventional Global Telecommunications System (GTS) data. We then examine the responses of the two control variable systems to radar DA through a more detailed study on one of the seven cases.

In section 2, we provide an overview of WRF 3DVar and describe the method to derive the background error statistics. In section 3, we compare the characteristics of the BE statistics of the $\psi\chi$ and UV control variables. The analysis increments from single-observation and real data experiments are compared in section 4. The impacts of the two pairs of control variables on precipitation forecasts of the seven summer convective cases are compared in section 5. In this section we also show results of one case that includes radar DA. The summary and conclusions are given in the final section.

2. Description of WRFVAR

a. Overview

WRFVAR employs the incremental variational formulation (Courtier et al. 1994) commonly applied in operational systems. The advantage of the incremental approach is that it not only reduces the computational cost but also improves the mathematical conditioning of the cost function (i.e., a quadratic cost function) because of the linearization of the forward operator. The incremental variational scheme minimizes a cost function defined as a function of the analysis increment relative to the background. The original nonlinear formulation of the cost function is written as

$$J = \frac{1}{2}(\mathbf{x} - \mathbf{x}_b)\mathbf{B}^{-1}(\mathbf{x} - \mathbf{x}_b) + [\mathbf{y}^o - \mathbf{H}(\mathbf{x})]^{\mathrm{T}}\mathbf{R}^{-1}[\mathbf{y}^o - \mathbf{H}(\mathbf{x})],$$
(1)

where the vectors $\mathbf{x}$, $\mathbf{x}_b$, and $\mathbf{y}^o$ represent the analysis variable, the background variable, and the observation variable, respectively; $\mathbf{B}$ is the background error matrix; and $\mathbf{R}$ is the observation error matrix. The variable $\mathbf{H}$ is the observation operator that maps the analysis or background variables from model space to observation space. With the typical number of grid points in numerical weather prediction (NWP) models, the background error covariance $\mathbf{B}$ is commonly a $10^7 \times 10^7$ matrix and its inverse is difficult to compute and, hence,

simplifications must be sought. Applying the matrix decomposition $\mathbf{B} = \mathbf{U}\mathbf{U}^{\mathrm{T}}$, the transforms

$$\mathbf{U}\mathbf{v} = \mathbf{x} - \mathbf{x}_b$$
(2)

and

$$\mathbf{d} = \mathbf{y}^o - \mathbf{H}(\mathbf{x}_b),$$
(3)

and the approximation

$$\mathbf{y}^o - \mathbf{H}(\mathbf{x}) \approx \mathbf{y}^o - \mathbf{H}(\mathbf{x}_b) - \mathbf{H}'(\mathbf{x} - \mathbf{x}_b)$$
(4)

to Eq. (1), the incremental formulation of the cost function is obtained and written as

$$J = \frac{1}{2}\mathbf{v}^{\mathrm{T}}\mathbf{v} + \frac{1}{2}(\mathbf{d} - \mathbf{H}'\mathbf{U}\mathbf{v})^{\mathrm{T}}\mathbf{R}^{-1}(\mathbf{d} - \mathbf{H}'\mathbf{U}\mathbf{v}).$$
(5)

The vector $\mathbf{v}$ is the control variable, the vector $\mathbf{d}$ is the innovation (observation minus background) vector that measures the departure of the observation $\mathbf{y}^o$ from its background $\mathbf{x}_b$, and $\mathbf{H}'$ is the linearization of the nonlinear observation operator $\mathbf{H}$. Note that the adjoint of $\mathbf{H}'$ is needed to calculate the gradient of the cost function.

Equation (2) is a preconditioning transform through which the direct computation of the inverse of the background matrix $\mathbf{B}$ is avoided. With this transform, the analysis increment

$$\delta\mathbf{x} = \mathbf{x} - \mathbf{x}_b = \mathbf{U}\mathbf{v} = \mathbf{U}_p\mathbf{U}_v\mathbf{U}_h\mathbf{v}$$
(6)

is obtained by applying the decomposed background matrix $\mathbf{U}$ to the control variable $\mathbf{v}$. The matrix $\mathbf{U}$ consists of a series of operations (Barker et al. 2004), $\mathbf{U}_p\mathbf{U}_v\mathbf{U}_h$, where $\mathbf{U}_h$ and $\mathbf{U}_v$ stand for the horizontal and vertical transforms, respectively, that essentially create horizontal and vertical autocorrelations of control variables. The variable $\mathbf{U}_h$ is realized through the application of a recursive filter (Hayden and Purser 1995). The determination of the correlation length scales used in the filter will be described later in this section. The vertical transform $\mathbf{U}_v$ is applied by an empirical orthogonal function (EOF) decomposition of the vertical component of background error covariance. The transform $\mathbf{U}_p$ converts the increment in control variable space to model variable space.

The most commonly used control variables in WRFVAR are streamfunction (ψ), unbalanced velocity potential (χ_u), unbalanced surface pressure (P_{su}), unbalanced temperature (T_u), and pseudo–relative humidity (RH_s) (water vapor mixing ratio divided by its saturated counterpart in the background field). The word "unbalanced" refers to the residual after a

statistical balance to the streamfunction is removed. This set of control variables (CV) is hereafter referred to as CV_$\psi\chi$. The transform $\mathbf{U}_p$ is defined as

$$\nabla^2\psi = \frac{\partial v}{\partial x} - \frac{\partial u}{\partial y} \quad \text{and} \quad \nabla^2\chi = \frac{\partial u}{\partial x} + \frac{\partial v}{\partial y}, \qquad (7)$$

or

$$u = \frac{\partial \psi}{\partial y} - \frac{\partial \chi}{\partial x} \quad \text{and} \quad v = \frac{\partial \psi}{\partial x} + \frac{\partial \chi}{\partial y}. \qquad (8)$$

In addition to the control variable conversion, $\mathbf{U}_p$ also involves the addition of the correlations between the streamfunction and other variables.

For this study, the new control variable option that directly uses the velocity components u and v is added to WRFVAR. For this new CV option, the operation $\mathbf{U}_p$ in Eq. (6) becomes an identity matrix. Hereafter, we refer to this new CV option as CV_UV. The control variables from the two CV options are summarized as

$$\text{CV\_}\psi\chi:\ \psi, \chi_u, P_{su}, T_u, \text{ and } \text{RH}_s,$$
$$\text{CV\_UV:}\ u, v, P_s, T, \text{ and } \text{RH}_s.$$

Note that the temperature and surface pressure are the full variables in CV_UV because it is assumed that the control variables are independent. In the next section, we will show that the correlations of u and v between themselves and with other variables are not significant. In CV_$\psi\chi$, however, a linear regression is used to compute and subtract the correlations between the streamfunction and the velocity potential, temperature, and surface pressure. Only the unbalanced part of the variable is used as the control variable. We could compare CV_UV with the CV_$\psi\chi$ without the consideration of the multivariate correlation. However, since it has been found that the impact of the multivariate correlation is not significant on the precipitation forecast using a similar configuration as in the current study (H. Wang 2013, personal communication), the WRFDA standard CV_$\psi\chi$ option that was a popular choice in previous studies is used in the current study.

b. Derivation of background error statistics

In section 2a we have shown that the background error covariance matrix $\mathbf{B}$ is modeled by a series of operations that results in the following approximation:

$$\mathbf{B} \approx \mathbf{U}_p \mathbf{U}_v \mathbf{U}_h \mathbf{U}_h^{\mathrm{T}} \mathbf{U}_v^{\mathrm{T}} \mathbf{U}_p^{\mathrm{T}}. \qquad (9)$$

To compute $\mathbf{B}$ using Eq. (9), a forecast error ensemble is needed that is obtained by the NMC method in this study. The NMC method was first introduced by Parrish and Derber (1992) and named after the National Meteorological Center, now called the National Centers for Environmental Prediction (NCEP). Although the method has its potential deficiencies (Errico et al. 2015), it is one of the most commonly used methods for variational data assimilation. The NMC method derives the climatological BE statistics from an ensemble of the differences between forecasts of two different lengths [hereafter called the forecast difference ensemble (FDE)], but valid at the same time. The forecasts are usually obtained by running a NWP model for at least a month. The dataset used to obtain the FDE is from the WRF 3-km real-time forecasts during May and June 2012 over a domain with the longitudinal and latitudinal distances about twice as large as the inner 3-km domain shown in Fig. 1b, which is the nested domain for the DA and forecast experiments that will be discussed in sections 4 and 5. The FDE was obtained by computing the difference between the 24- and 12-h model forecasts valid at the same time using this dataset, yielding 60 ensemble members. From this FDE, statistics such as variance and length scale can be obtained.

To compute the variance and length scale for ψ and χ from the FDE, the streamfunction and velocity potential need to be calculated first by the inverse Laplacian implied by Eq. (7) from the model-forecasted u and v. Although the conversion between UV and $\psi\chi$ is reversible (this property has been checked for WRFVAR) as long as the boundary conditions for ψ and χ are correctly specified, the background error statistics can be altered, as will be shown in the next section. For the current study we used the WRFVAR utility gen_be to generate the BE statistics. The reader can refer to WRFDA Users' Guide (http://www2.mmm.ucar.edu/wrf/users/wrfda/index.html) for detailed description of the computation method. Referring back to Eq. (9), we can see that the background error covariance is decomposed into the horizontal and vertical components. The horizontal covariance is realized through a recursive filter using the length scales and variances obtained in the above procedure, while the vertical covariance is achieved by the vertical covariance decomposition. Hence, both the variance and the length scale generated by gen_be are a function of the K EOF modes, where K is the number of the model vertical levels.

3. Comparison of the background error statistics

In this section, we compare the forecast error statistics of the momentum variables for CV_$\psi\chi$ and CV_UV obtained from the NMC FDE. In addition to physical considerations, a requirement in choosing control
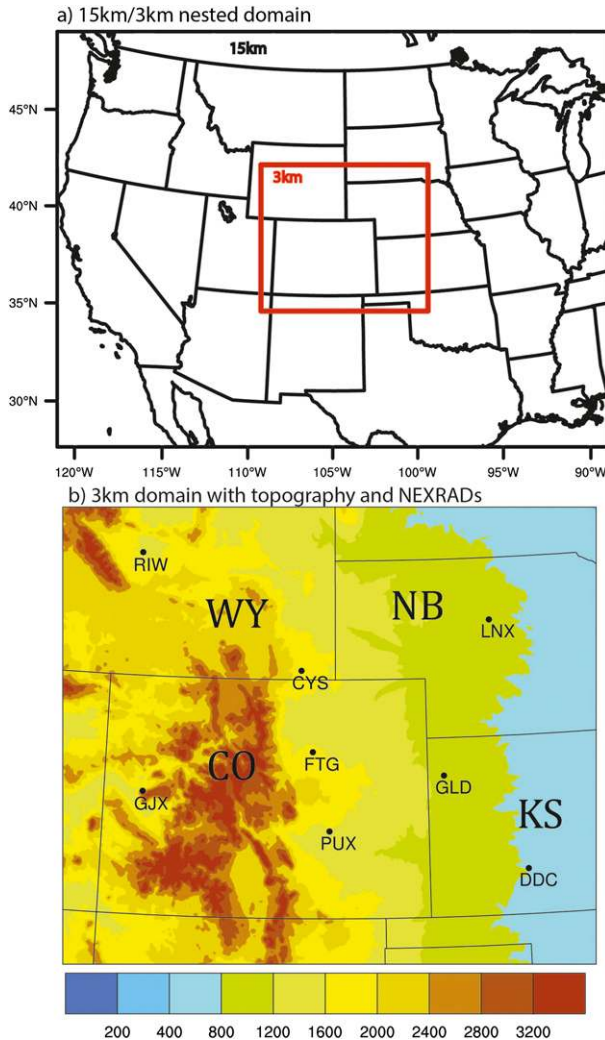
FIG. 1. (a) The 15/3-km nested domain for data assimilation and forecast experiments. (b) Enlarged 3-km domain with topography and locations of NEXRADs used in the case study of the 9 Aug 2008 event. The states of Colorado, Kansas, Wyoming, and Nebraska are also marked in (b).

variables is that their errors are similar to that of a Gaussian error distribution, because this assumption is applied in deriving the 3DVar cost function in Eq. (1) (Lorenc 1986). Therefore, we first examine the characteristics of error distributions of the two pairs of control variables. Figure 2 shows the error distributions of the four momentum variables ψ, χ, u, and v. It is evident that all four variables display approximately Gaussian-distributed error structures.

To see how the two pairs of momentum variables correlate with each other and with other variables, correlation coefficients of ψ, χ, u, and v on each vertical level are calculated from the FDE and shown in Fig. 3. The vertical distributions of the correlations between

the momentum pairs are shown in Fig. 3a and between temperature, pressure, and relative humidity and the four momentum variables are shown in Figs. 3b, 3c, and 3d, respectively. From Fig. 3a, we first observe that the correlation between ψ and χ is significantly greater than that between u and v, especially on the low levels. Figure 3c shows that the correlation between the pressure and the velocity components u (or v) is negligible for all levels. In contrast, and as expected, significant correlation is seen in the low levels between pressure and ψ (or χ), presumably due to the geostrophic balance. The velocity components u and v are generally less correlated with temperature than are ψ and χ (Fig. 3b) except for the top levels above 200 mb (1 mb = 1 hPa). The correlations of relative humidity are largest with u below 400 mb and the larger correlations occur at higher levels with ψ and χ.

The small correlations between u and v and between wind and pressure suggest that there is not an obvious climatological balance between these two momentum variables, and thus it is justifiable to treat these variables independently without consideration of multivariate correlation. For temperature and humidity, however, there could be some benefit to model the small correlations with wind, although we have chosen to ignore them in the current study. In contrast to CV_UV, the correlations in CV_$\psi\chi$ are relatively larger, especially between ψ and χ and between ψ (or χ) and pressure, which can be regarded as a justification for the application of multivariate correlation modeling. Following Wu and Purser (2002) and Barker et al. (2004), the multivariate correlation in CV_$\psi\chi$ is estimated by a statistical regression using the data from FDE. The use of the $\psi\chi$ control variables provides a way to take into account the geostrophic balance, which is important for data assimilation systems aimed primarily at resolving large-scale motions. However, for a nonhydrostatic model resolving high-resolution flows, we question whether CV_$\psi\chi$ is the best way to consider the large-scale geostrophic balance. In the following, we will show that CV_$\psi\chi$ has some BE properties that may produce a negative impact on 3DVar analysis when a limited-area nonhydrostatic model is used.

Although no multivariate correlation is considered in CV_UV in the current study, we are not suggesting that it is not important to account for the multivariate balance. Rather, the purpose of this study is to point out some potential problems of the $\psi\chi$ control variable scheme in the context of high-resolution data assimilation when large amounts of data (e.g., from radar and mesonet) are used with a nonhydrostatic model. These types of high-resolution models have the capability to resolve the multiscale atmospheric flows that cannot be
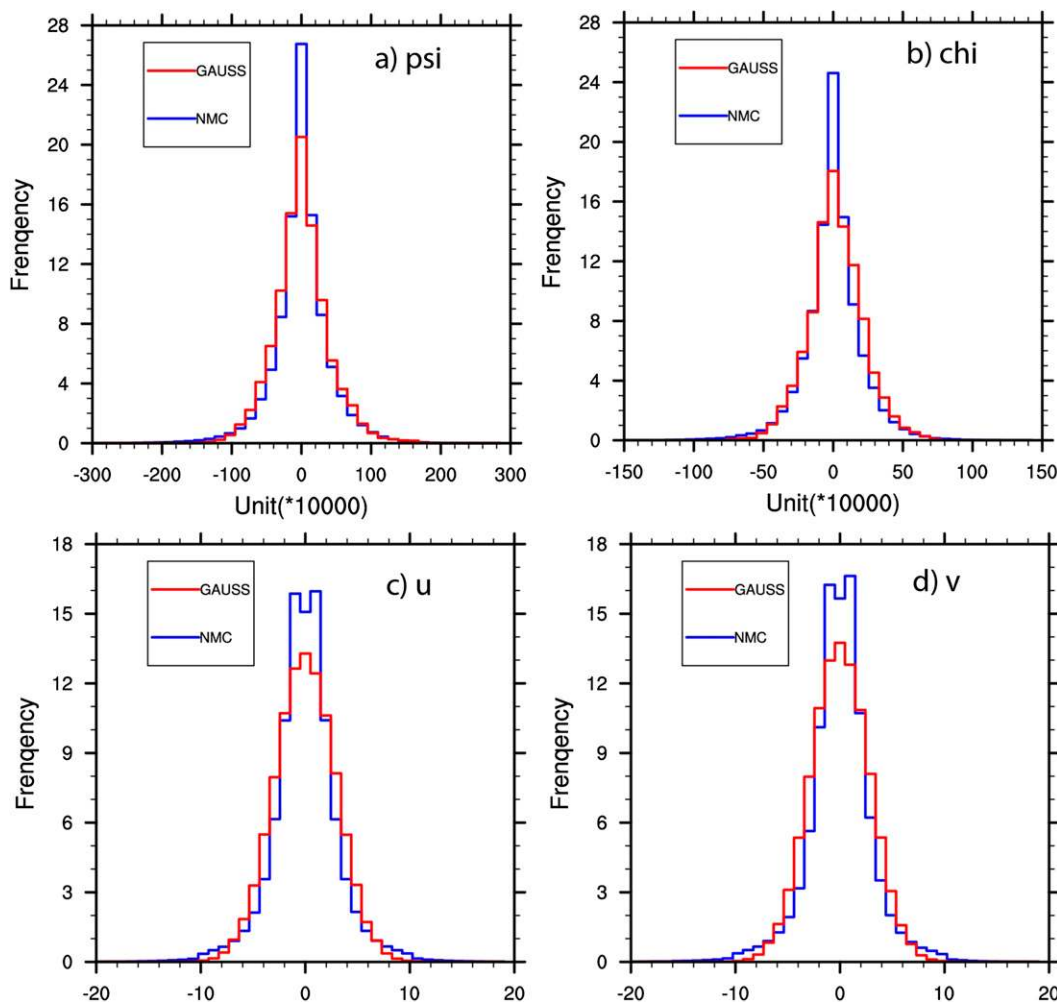
FIG. 2. Forecast error distributions of (a) streamfunction ψ, (b) velocity potential χ, (c) u wind, and (d) v wind as estimated using the NMC method (blue) and by the Gaussian function (red).

described by any specific balance approximations. We believe that for regional data assimilation with plentiful high-resolution observations a large portion of the multivariate balance should be extracted from the observations, although it is still necessary to include balance constraints, which can be important for undersampled regions. Approaches are being sought by adding appropriate constraints in the cost function (penalty function) that can account for the multivariate balance suitable for convective-scale data assimilation. The penalty function method of adding multivariate constraints has been shown to be effective in meso- and convective-scale variational data assimilation systems (Xie et al. 2002; Ge et al. 2012).

The BE statistics of variance and length scale for both momentum control variable options are derived based on homogeneous and isotropic assumptions, so they only vary with height. As mentioned previously, the vertical variation is represented by an EOF decomposition in the vertical, and we can thus plot the length scale and variance in terms of the EOF mode. In Fig. 4a, a plot of these length scales is displayed and it is shown that the length scales of u and v are smaller than those of ψ and χ. Also plotted in Fig. 4a are the length scale ratios between the momentum variables as a function of the EOF mode, as shown by the black dotted (for the length scale ratio between ψ and u) and dashed (for the length scale ratio between χ_u and u) lines. These two ratios increase as the wavenumber increases (except for modes 3–6), suggesting that the BE of $\psi\chi$ results in larger length scales for small-scale features in the atmosphere compared to that of UV. When the eigenvalues (indicating the variance explained by each EOF mode) are plotted with respect to the vertical wavenumbers (Fig. 4b), we can see that the ratio between ψ (or χ) and u decreases as the wavenumber increases,
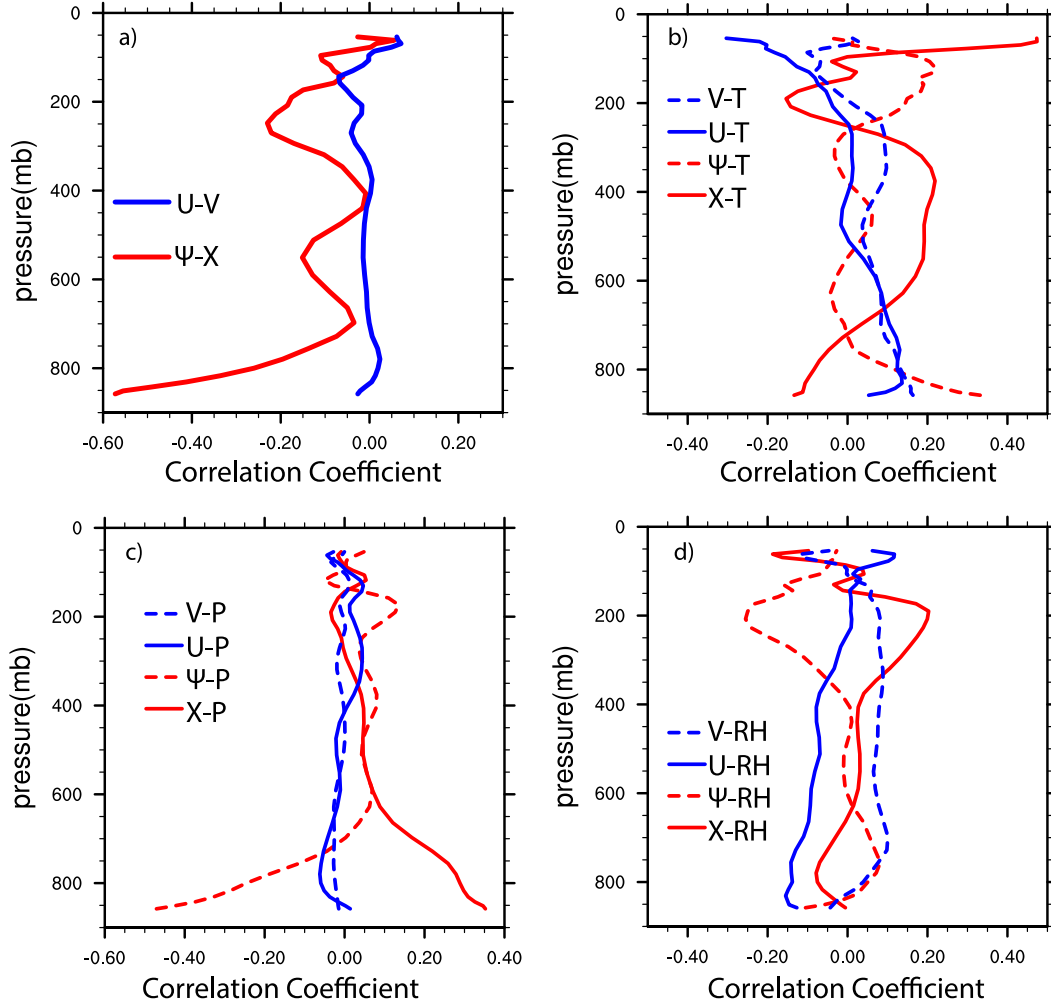
FIG. 3. (a) Vertical distribution of correlation coefficients between u and v (blue) and between ψ and χ (red). (b) Vertical distribution of correlation coefficients between T and v (dashed blue), T and u (solid blue), T and ψ (dashed red), and T and χ (solid red). (c) As in (b), but for pressure P. (d) As in (b), but for relative humidity RH.

opposite to the trend for the length scale. Note that the eigenvalues plotted in Fig. 4b are scaled by their respective first mode to equalize the scales for the ease of plotting. Figure 4 suggests that the variable transformation between UV and $\psi\chi$ acts as a smoother that enlarges the length scale and reduces the variance and that the smoothing impact increases as the wavenumber increases. That finding is easily understandable if we examine Eq. (6) in terms of spectral decomposition:

$$\nabla^2\psi \propto (k^2 + l^2)\overline{\psi} = F, \qquad (10)$$

where F represents the right-hand side of Eq. (7), $\overline{\psi}$ is the Fourier expansion of ψ, and k and l are wavenumbers in the x and y directions, respectively. Equation (10) clearly shows that $\overline{\psi}$ is inversely proportional to the horizontal wavenumbers. If we assume the dominant

motions in the atmosphere are three dimensional, meaning that the magnitude of the horizontal scale is positively correlated with that of the vertical scale, Eq. (10) can be used to explain the scale dependence of the BE statistics between the two control variable options displayed in Fig. 4.

The above comparison of the BE statistics of the momentum control variables in spectral space provides some insight, but we also want to see, in physical space, the differences of the u and v error statistics resulting from the two CV options. To do that, we generated u and v ensembles of 200 members via a Gaussian re-sampling process (Wang et al. 2014) using the BE variances and length scales from CV_UV. Similarly, 200 ψ and χ ensembles were generated using those statistics from CV_$\psi\chi$, and then the ψ and χ ensemble fields were converted to u and v fields using Eq. (8) after the
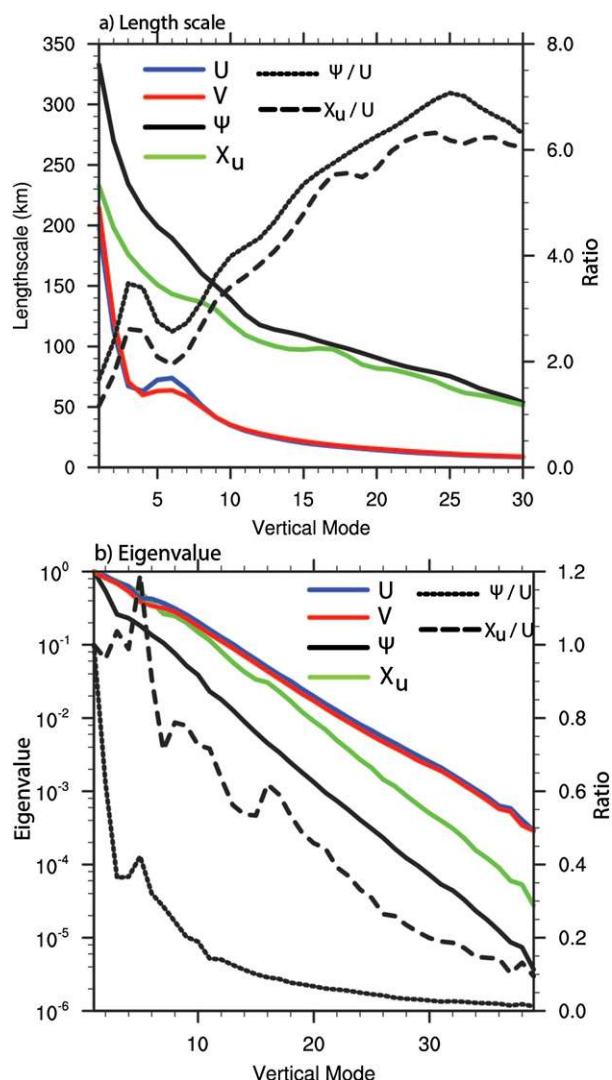
FIG. 4. (a) Length scale plotted as a function of vertical mode for ψ (black), χ_u (green), u (blue), and v (red). The length scale ratios between ψ and u and between χ_u and u are shown by dotted and dashed lines, respectively. (b) As in (a), but for eigenvalue scaled by the first mode.

balanced part between ψ and χ is added back. From these two groups of ensembles, the spatial correlations of u and v can be computed for the two CV options. The spatial correlations are also directly calculated from the NMC FDE and used as truth in the following comparison. By comparing the spatial correlation and STD calculated from the resampled ensembles for the two CV options against those computed directly from NMC FDE, we can evaluate how the BE modeling procedure summarized in the last section can alter the spatial correlations of the velocity components. For simplicity, in the following, the direct calculation of the error statistics from the NMC FDE will be referred to as NMC.

Figure 5 shows the u-wind (Figs. 5a,b) and v-wind (Figs. 5c,d) correlations from CV_$\psi\chi$, CV_UV, and NMC along the west–east (Figs. 5a,c) and north–south (Figs. 5b,d) directions on the ninth vertical model level, which is close to 700 mb. The results suggest that CV_$\psi\chi$ gives much larger decorrelation distances than that from NMC, while CV_UV yields substantially smaller decorrelation distances than CV_$\psi\chi$ but still larger than NMC. Another notable aspect that can be observed from Fig. 5 is that the u-wind correlation along the y direction and the v-wind correlation along the x direction from CV_$\psi\chi$ have negative values at long distance, which is not shown by the direct calculation from NMC FDE. When the length scales of CV_$\psi\chi$ are reduced by half, the resulting spatial correlations are very close to those from CV_UV for the u wind along the x direction and the v wind along the y direction (thin dashed lines denoted by CV_$\psi\chi$0.5 in Fig. 5); however, the negative tails are amplified for the u-wind correlation along the y direction and the v wind along the x direction. Wang et al. (2014) found similar unrealistic negative correlations at long distance from CV_$\psi\chi$ using a NMC FDE from China in their study to design an inhomogeneous BE covariance for WRFVAR. This finding suggests that, although the enlarged length scales in CV_$\psi\chi$ can be reduced by an artificial tuning, the practice can result in unrealistic correlations at long distance, posing another potential problem.

4. Comparison of analysis increments

a. Single-observation experiments

One simple way to examine the effect of the BE statistics in physical space is via a single-observation test. Such a test was performed by placing a single observation of u with an innovation (difference between observation and background) of $1\,\mathrm{m\,s^{-1}}$ on the 20th model level in the middle of the inner analysis domain shown in Fig. 1. CV_$\psi\chi$ and CV_UV can result in different u increments due to their different BE covariance matrices. The background field for the single-observation experiments is the North American Mesoscale Forecast System (NAM) analysis at 0000 UTC 9 August 2008, which is the case that will be studied in more detail in section 5. With the background and the single observation, WRF 3DVar was run with both control variable options CV_$\psi\chi$ and CV_UV and their respective BE statistics.

The increments of u from the experiments using CV_$\psi\chi$ and CV_UV are shown in Figs. 6a and 6b, respectively, plotted in the x–z plane through the observation point. The area of the positive increment is much larger from the experiment CV_$\psi\chi$ (Fig. 6a) than that
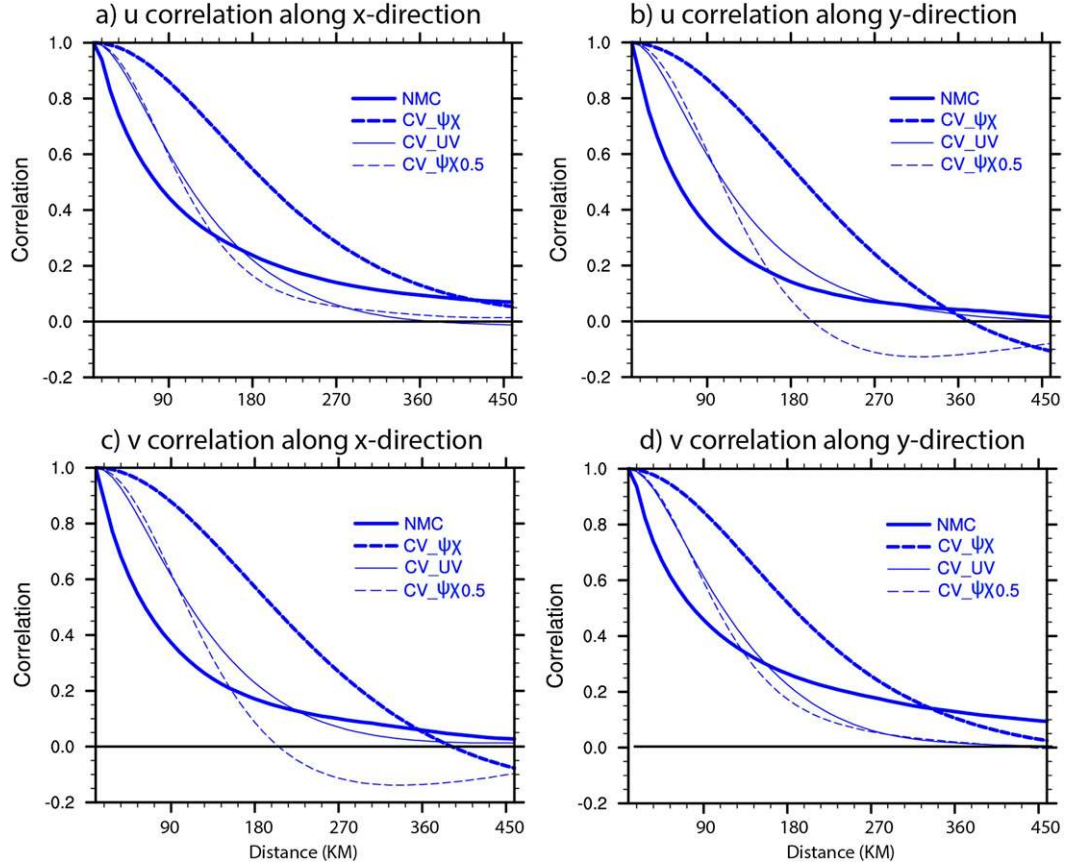
FIG. 5. Horizontal correlations on the ninth model level (about 700 mb) for u along the (a) x direction and (b) y direction, and for v along the (c) x direction and (d) y direction. The four lines represent correlations directly calculated from the NMC FDE (thick solid), recomputed from ψ and χ BE statistics (thick dash) and u and v BE statistics (thin solid), and recomputed from ψ and χ BE statistics but with half of the length scale (thin dash).

from CV_UV (Fig. 6b) in terms of the horizontal spread. The smoothing effect of CV_$\psi\chi$ is more clearly seen in Fig. 6d where the increment profiles from the two experiments along the blue line in Fig. 6a and the red line in Fig. 6b are compared. It shows that the increment of u from CV_UV has a larger magnitude and smaller horizontal spread than that from CV_$\psi\chi$.

Since the correlation between ψ and χ, T, and P_s are accounted for in CV_$\psi\chi$, the observation of u not only results in u increments but also in increments of v, T, and P_s. However, it is noted that the values of these increments are relatively insignificant. The maxima of the increments for v, T, and P_s are $0.06\,\mathrm{m\,s^{-1}}$, $0.03°\mathrm{C}$, and $0.057\,\mathrm{hPa}$, respectively, in response to the $1\,\mathrm{m\,s^{-1}}$ innovation of u. Figure 6c shows the temperature increment on the y–z plane through the observation point. Clear patterns are obtained due to the balance correlation between ψ and T in the CV_$\psi\chi$ BE, but the magnitude is very small. There are no v, T, and P_s increments produced by CV_UV because no climatological correlations

are considered between u and these variables. The humidity field is independent in both CV schemes, so there are no increments in response to the $1\,\mathrm{m\,s^{-1}}$ innovation of u.

b. Comparison of increments using real data

The increments from CV_$\psi\chi$ and CV_UV are also compared when synoptic observations from GTS are assimilated with the same background as in the single-observation experiments. Figure 7 shows the u, T, and q_v increments on the sixth model level from the 3DVar experiments using CV_$\psi\chi$ (left column) and CV_UV (right column). The most striking difference occurs in the u-increment fields where the CV_$\psi\chi$ experiment (Fig. 7a) produces a much smoother increment than the CV_UV experiment (Fig. 7b) in which more small-scale features are analyzed. Both experiments yield larger increments over the high terrain of the Rocky Mountains in Colorado; however, the increment field from the CV_UV experiment shows a north–south pattern
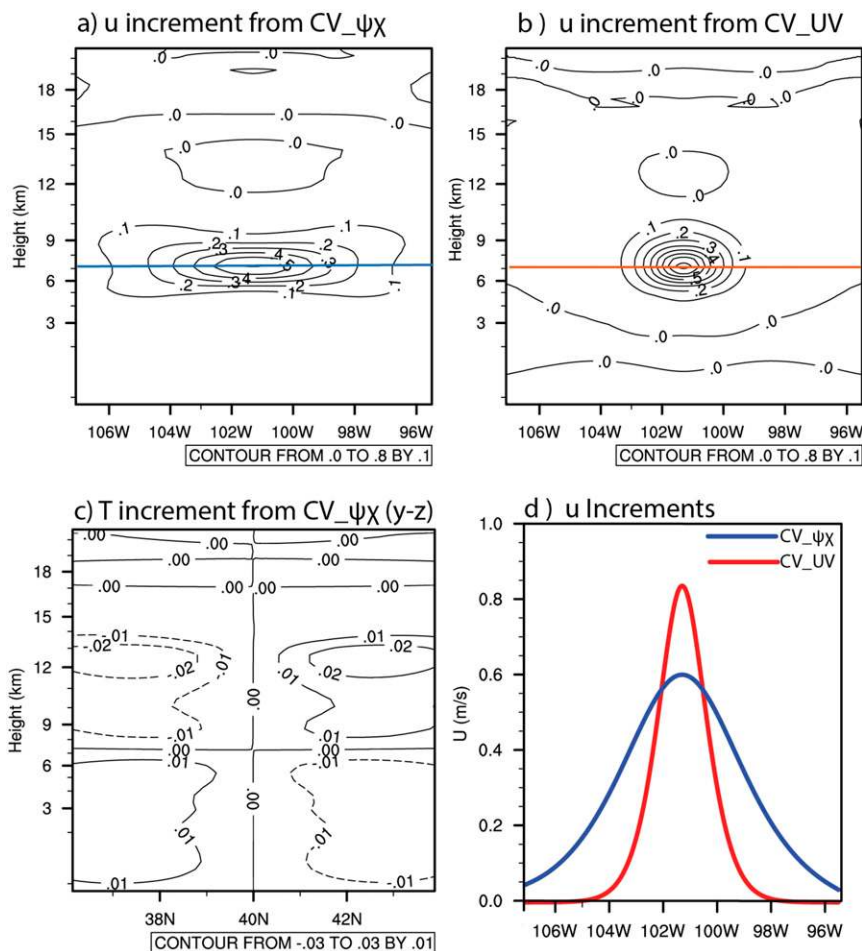
FIG. 6. Vertical x–z cross sections of u analysis increment from the single-observation experiments using (a) CV_$\psi\chi$ and (b) CV_UV. Vertical y–z cross section of T analysis increment from the single-observation experiment using (c) CV_$\psi\chi$. (d) The profiles of the increments of u along the blue line in (a) (blue) and along the red line in (b) (red) on the level where the single observation is assumed. Note that in the plots (a),(b), and (c) the vertical coordinate is the WRF sigma level labeled by the corresponding height in km.

that is in better agreement with the orographic orientation. The temperature increments from the two schemes are quite similar. Since the only difference between the two CV options for the temperature is that CV_$\psi\chi$ considers the correlation between ψ and T through a linear regression, the differences in the temperature increments represent the impact of the multivariate balance. The humidity increments are exactly the same since both CV options treats the humidity variable independently.

It is not surprising to observe the large differences between the velocity increments from the two CV options given their significant differences in the velocity error statistics presented in section 3. Although it is possible to artificially reduce the length scales of ψ and χ to obtain a velocity increment with some smaller-scale structures, it can cause nonphysical errors as shown

in section 3, and it could violate the statistical multivariate balance that is consistent with the untuned BE. In section 5, we will show in a case study that reducing the length scale does not improve the analysis and forecast either.

5. Impacts of control variables on precipitation forecasts

a. Results from multiple-case experiments

Multiple historical convective cases that caused flash floods over the region of the Rocky Mountain Front Range were selected and employed in the current study as part of a collaborative project on the study of flash flood prediction in this region. The WRF 3DVAR
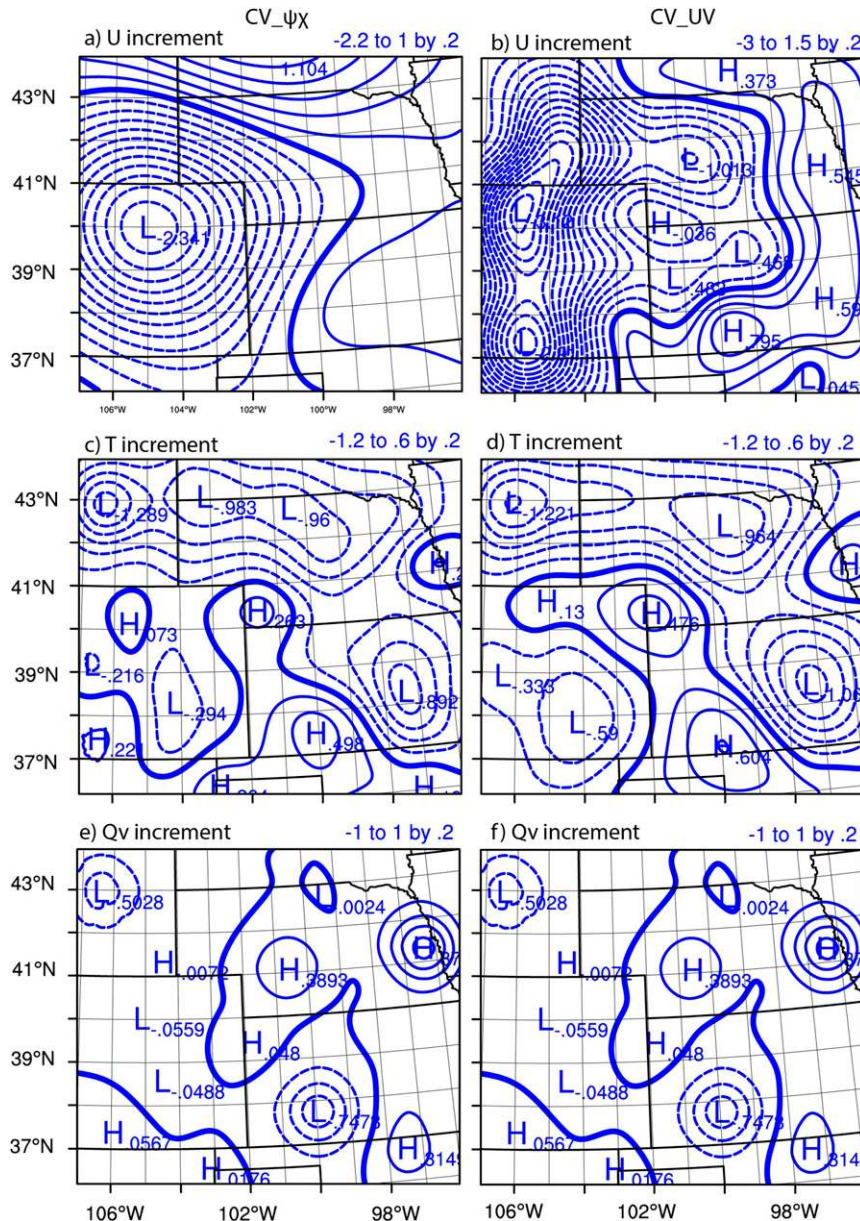
FIG. 7. Analysis increments of (a),(b) u (m s^{-1}); (c),(d) T (°C); and (e),(f) q_v (g g^{-1}) on the sixth model σ level (approximately 800 mb) at 1200 UTC 8 Aug 2008 from the real data experiments using (left) CV_$\psi\chi$ and (right) CV_UV.

model was run for seven cases using both control variable options in order to examine their sensitivities on quantitative precipitation forecasts (QPFs). Table 1 lists the dates and main high-impact weather features of the seven cases. For each of these cases, WRF 3DVAR was run with continuous 3-h analysis cycles, and 0–12-h forecasts were produced at 0000, 0600, 1200, and 1800 UTC initialization times. The nested domains shown in Fig. 1a were used for these runs. The inner domain is enlarged in Fig. 1b to show the topography

and the locations of eight radars used in the case study discussed later in this section. There are a total of 51 vertical levels used in the WRF forecast model.

The multiple-case runs assimilate GTS data, including radiosonde and aircraft data, surface synoptic observations (SYNOP), automated weather station observations (AWS), and the global positioning system precipitable water (GPS PW). The starting and ending times for each case vary depending on the occurrence time of the major convective systems on the analysis

Date	Description
8–9 Aug 2008	Flooding with fatality in south Denver
3–4 Jul 2009	Large hailstorm in north Denver
28 Jul 2010	Heavy hailstorm in Nederland
16 Aug 2010	Boulder thunderstorm
13–14 Jul 2011	Fourmile Canyon flood
6–7 Jun 2012	Widespread heavy rain over foothills
7–8 Jul 2012	Widespread heavy rain over Front Range

domain. There are 29 (in total) 0–12-h forecasts for the 7 cases. The boundary conditions for the 15-km outer domain are provided by the NAM forecast. The Kain–Fritsch cumulus parameterization scheme is used only in the outer domain. Other physics options are the Thompson bulk microphysics scheme, the Mellor–Yamada–Janjić (MYJ) PBL scheme, the Monin–Obukhov surface layer scheme, and the RRTMG radiation scheme. The description of the above schemes can be found in the ARW technical report (Skamarock et al. 2008).

Since the main purpose of the multiple-case studies on the chosen domain is to assess the system performance in terms of QPF, our statistical analysis focuses on precipitation skills over the 29 forecasts. The respective QPF skill, as represented by the fractions skill score (FSS) with a radius of influence of 9 km, from the two analysis and forecast runs using CV_$\psi\chi$ (named EXP_$\psi\chi$) and CV_UV (named EXP_UV) are compared in Fig. 8 for the hourly accumulated precipitation thresholds of 1 (Fig. 8a) and 5 mm (Fig. 8b). The stage-IV precipitation analysis, a multisensor rainfall product produced by NCEP (Lin and Mitchell 2005), is used as the observation in the computation of the FSS. Improvement of the QPF skill is evident for the higher threshold over the entire 12 forecast hours, while improvement for the lower threshold occurs mostly during the later forecast hours. The trend of decreasing QPF skill for both thresholds in the later hours shown for EXP_$\psi\chi$ is appreciably corrected by EXP_UV. To test whether the difference between the two runs is statistical significant, the mean FSS difference and its 95% confidence interval are calculated for both thresholds and the results are written on the two figure panels, respectively. The results indicate that the difference well passes the significance test for the higher threshold and barely passes it for the lower threshold.

By examining the forecast precipitation patterns of the 29 forecasts over the seven cases, we found that EXP_UV had the most positive impact on QPF for forecasts of organized convective systems. In Fig. 9, some results of the forecasts from EXP_$\psi\chi$ (middle column) and EXP_UV
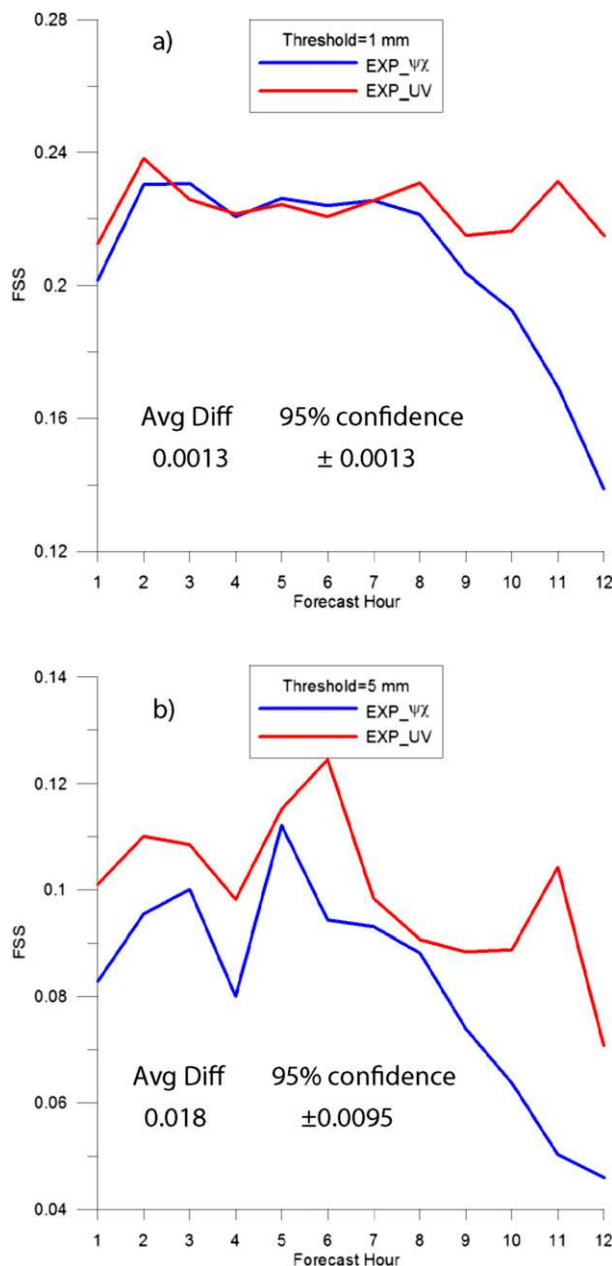

FIG. 8. Fractions skill scores with 9-km radius of influence for the hourly precipitation thresholds of (a) 1 and (b) 5 mm aggregated over 29 forecasts, from the experiments EXP_$\psi\chi$ (blue) and EXP_UV (red). The standard deviations (STD) of the FSSs (over all forecast hours and all cases) are shown for both experiments (red for EXP_UV and blue for EXP_$\psi\chi$).

(right column) are shown and verified by the stage-IV precipitation analysis (left column).

On 28 July 2010 (Figs. 9a–c), scattered convection occurred in the area of the Rocky Mountain Front Range, and a storm near Nederland, Colorado, produced heavy rain and hail. The two forecasts do not show significant differences for this case, and they both
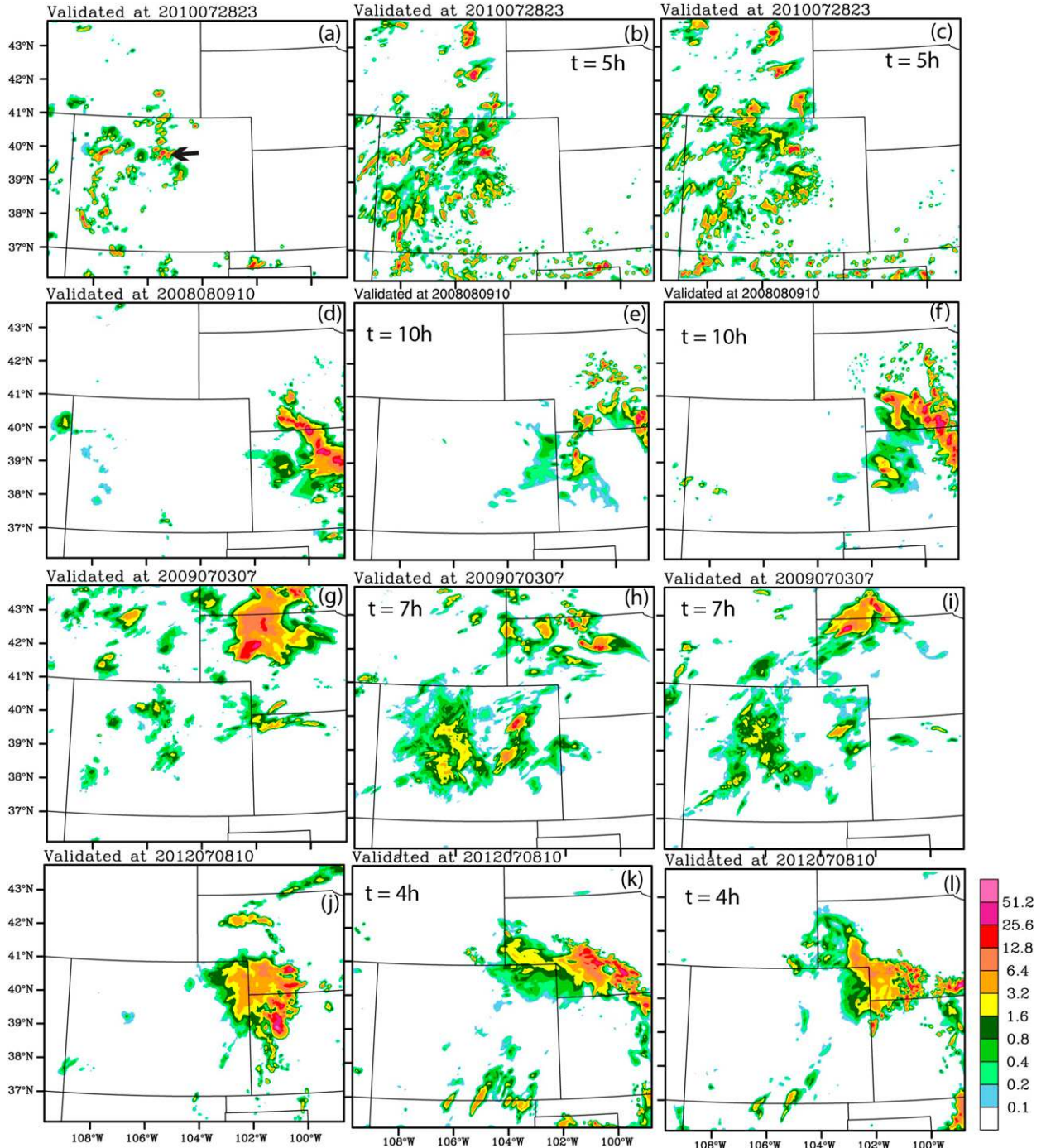
FIG. 9. Forecasts of 1-h accumulated precipitation for four different cases. (left) The stage-IV analyses, (middle) the forecasts from EXP_$\psi\chi$, and (right) the forecasts from EXP_UV. (from top to bottom) Forecast valid times are at 2300 UTC 28 Jul 2010, 1000 UTC 9 Aug 2008, 0700 UTC 3 Jul 2009, and 1000 UTC 8 Jul 2012. The forecast length for each case is labeled on the panel.

produced false alarms at various locations, although the deep storm that resulted in heavy rain and hail is forecasted by both experiments. This example typifies the cases of isolated convection that have less sensitivity to the selection of control variables. We believe that the reason for the low sensitivity in these cases is that the isolated storms cannot be well resolved by the 3-km model resolution.

The second case shown by Fig. 9d occurred on 9 August 2008. The 12-h forecast of EXP_UV (Fig. 9f)

starting at 0000 UTC predicts the organized line of convection quite well, while in contrast EXP_$\psi\chi$ (Fig. 9e) failed to forecast the organized convective system. The third case shown by Fig. 9g occurred on 3 July 2009. Similar to the previous case, the experiment with EXP_$\psi\chi$ fails to organize the storms near the border of Nebraska and South Dakota. For the last case shown by Fig. 9j, which occurred on 8 July 2012, the experiment of EXP_$\psi\chi$ predicts an organized convective system, but the location is too far to the northeast; while the forecast by EXP_UV produces a system that is in closer agreement with the observed system in terms of its orientation and location.

From these QPF examples, we can see that the EXP_UV control variables produce analyses that result in improved precipitation forecasts, especially for organized convective systems. In other words, the forecasts from EXP_UV are able to organize the convection when organized convective systems exist in the domain. The larger FSS values tend to be associated with more organized systems that have higher predictability in general. Overall, the EXP_$\psi\chi$ forecasts have more spurious convection and, hence, result in a larger false alarm rate (FAR), which is confirmed by the statistics of FAR over the 29 forecasts shown in Fig. 10. The largest reduction of FAR is for the higher precipitation threshold (5 mm, Fig. 10b). For the lower precipitation threshold, the main improvement is only for the long forecast ranges. The statistical significance test results (shown on the figure panels) also indicate that the difference is significant for the higher threshold, but not for the low threshold.

b. Case study of 9 August 2008

To gain more insight into the impacts of the two pairs of momentum control variables on analysis and forecast, we conducted a case study on the 9 August 2008 event. An emphasis here is to examine how the two control variable schemes behave when radar observations are assimilated. On this day, a cluster of storms initiated in Wyoming in the early afternoon (Fig. 11a) and organized into a convective line as the storms approached Colorado in the late afternoon (Fig. 11b). As the convective system passed through the Denver area, its southwest end collided with a mesoscale convergence feature (marked by the black arrow in Fig. 11c) and initiated a deep storm that resulted in flooding in Denver. The major system then dissipated as it moved out of Colorado. Note that a secondary convective band developed in Kansas between 0300 and 0500 UTC.

For this case study, we compare the impacts of the two control variable options without (EXP_$\psi\chi$ and EXP_UV) and with (EXP_$\psi\chi$_RA and EXP_UV_RA)
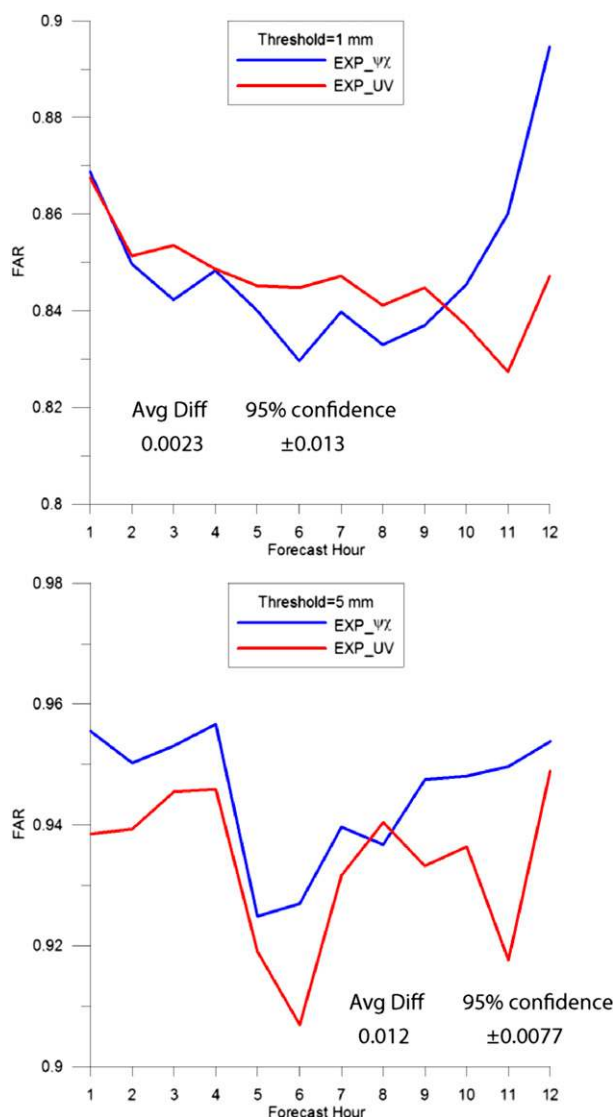

FIG. 10. As in Fig. 8, but for the false alarm rate.

radar observations. Both radial velocity and reflectivity data from the eight radars shown in Fig. 1b are assimilated using the scheme developed by Xiao et al. (2005) for radial velocity and Wang et al. (2013a) for reflectivity. The radar data are assimilated at 0000 and 0300 UTC 9 August 2008, and 0–12-h forecasts are launched at 0300 UTC. The 3DVar analysis at 0000 UTC from the multiple-case studies described above is used as the background.

We examined the fitting of the 3DVar analysis to the observations ($O - A$), where A represents the 3DVar analysis and O is the observation, and found that the largest difference occurred in the fitting to radial velocity. Figure 12 compares the ratio between the root-mean-square of ($O - A$) and that of ($O - B$) for radial
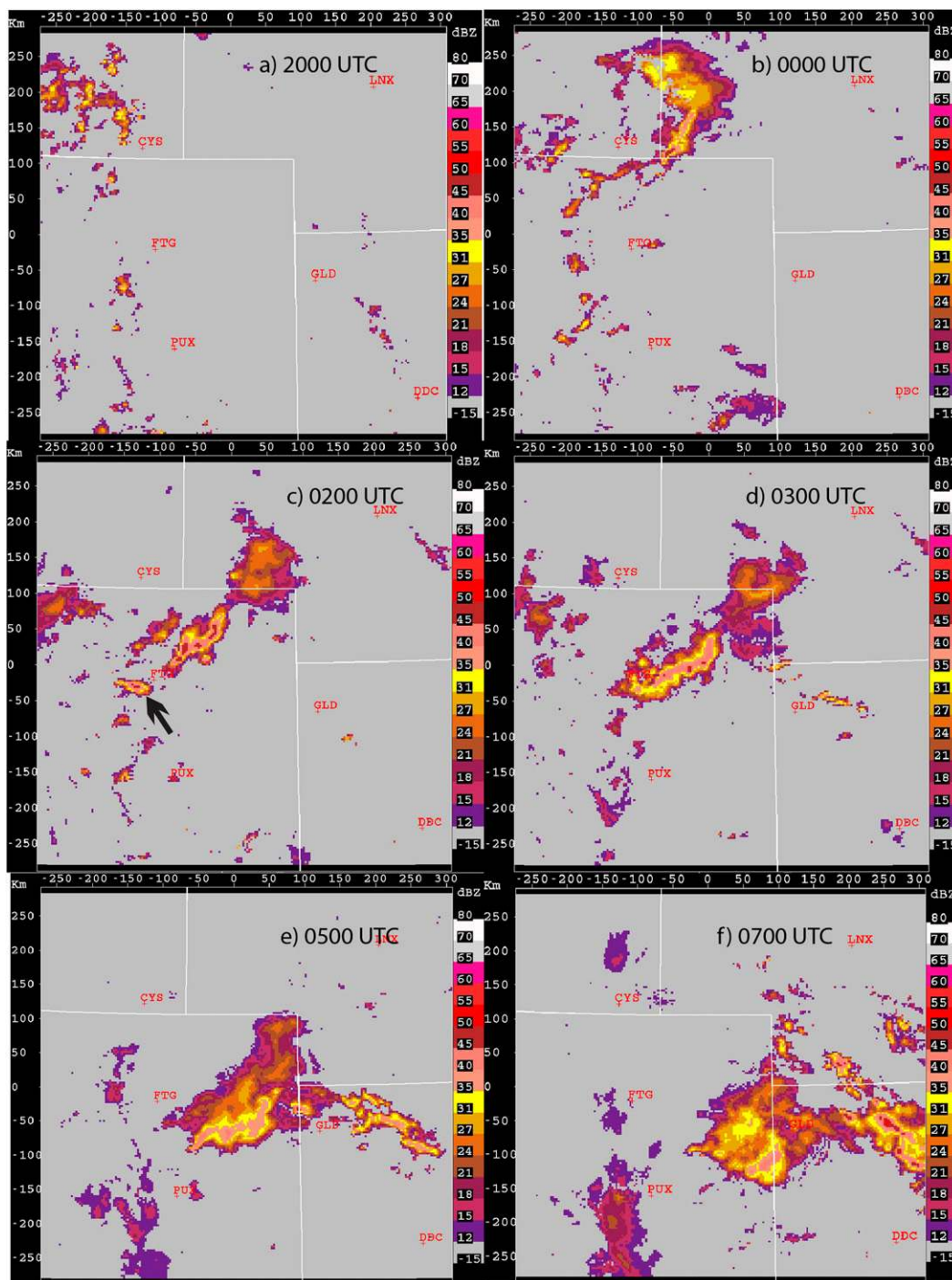
FIG. 11. Mosaic of first-elevation reflectivity using the NEXRADs KCYS, KFTG, KPUX, KDDC, KRIW, KGJX, and KGLD (see Fig. 1b for their locations) at (a) 2000 UTC 8 Aug 2008, and (b) 0000, (c) 0200, (d) 0300, (e) 0500, and (f) 0700 UTC 9 Aug 2008.

velocity at 0300 UTC, where B stands for the first-guess background (WRF forecast initialized at 0000 UTC with radar DA). The results clearly indicate that the analyzed radial wind from EXP_UV_RA fits much closer to the

observation than that from EXP_$\psi\chi$_RA. Tuning of the length scale and variance improves the fit in both experiments; however, it does not change the fact that EXP_UV_RA results in a closer fit to the radial velocity
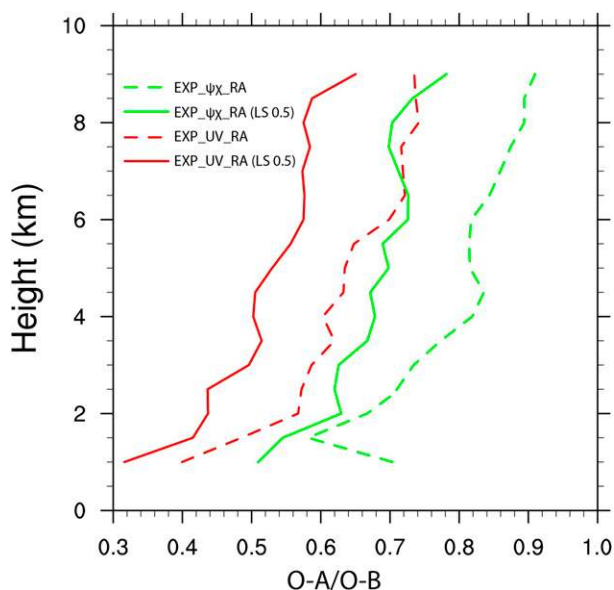
FIG. 12. Ratio between $O - A$ and $O - B$ where $O - A$ is the root-mean-square difference between the observed and the analyzed radial velocity and $O - B$ is the root-mean-square difference between the observed and the background radial velocity. The solid lines are results from the experiments with halved length scales (LS).

observations than EXP_$\psi\chi$_RA. Figure 12 shows an example of halving the length scales; it reveals that the tuning improves the fitting for both experiments (cf. the solid lines with the dashed lines), but EXP_UV_RA results in a closer fit to the observation than EXP_$\psi\chi$_RA. Nevertheless, a closer fit to observations does not necessarily mean an improved analysis. One way to evaluate the quality of the analysis is to verify the forecast from that analysis—an accurate and well-balanced

analysis should result in an improved forecast. Below we compare and verify the precipitation forecasts from the four experiments without and with radar observations. Wind forecasts will also be verified later in this section. For the radar experiments, we use those with halved length scales to improve the fitting to radar observations (refer to Fig. 12 and a discussion later), despite the fact that reducing the length scale can result in negative correlations at long distance. Further reduction of the length scales or increase of the variances were attempted for EXP_$\psi\chi$_RA, but did not result in significant change of $(O - A)$ and rather had the tendency to cause an adverse effect on precipitation forecast.

The FSSs for the precipitation threshold of 1 mm are compared in Fig. 13a for the no-radar experiments and in Fig. 13b for the radar experiments. For the no-radar experiments, the two forecasts have comparable forecast skills before $t = 7$ h and EXP_UV has a higher skill after that. With the radar DA, the skills for both EXP_UV_RA and EXP_$\psi\chi$_RA are increased from their counterparts without the radar DA up to $t = 4$ h, but beyond that, the FSS from EXP_UV_RA maintains a higher skill than EXP_UV except for the last hour; in contrast, the FSS from EXP_$\psi\chi$_RA decreases reaching a lower skill than EXP_$\psi\chi$ for most of the remaining forecast hours.

When the precipitation patterns between EXP_$\psi\chi$_RA and EXP_UV_RA are compared, it is seen that an organized precipitation band is forecasted as early as $t = 1$ h by EXP_$\psi\chi$_RA (Fig. 14c); however, there are substantial false alarms. In contrast, the results from EXP_UV_RA (Fig. 14d) agree better with the stage-IV analysis (Fig. 14a) both in terms of the area coverage
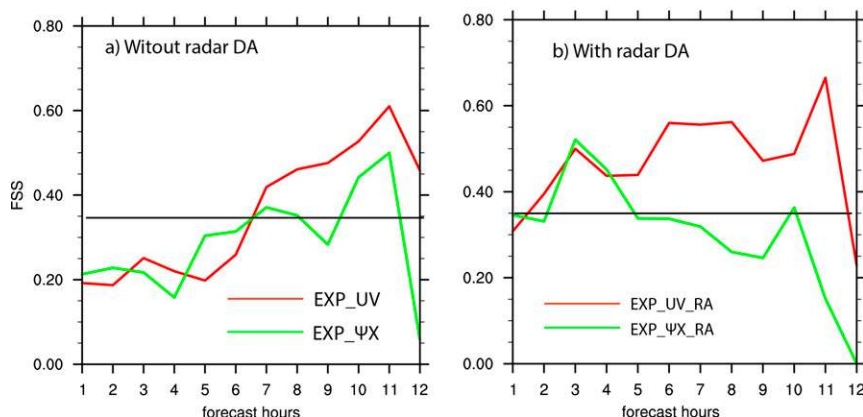

FIG. 13. Fractions skill scores with 9-km radius of influence for the hourly precipitation threshold of 1 mm from the experiments (a) without radar data assimilation and (b) with radar data assimilation. The horizontal black lines are drawn at the FSS level of 0.35 for the purpose of easy comparison between (a) and (b).
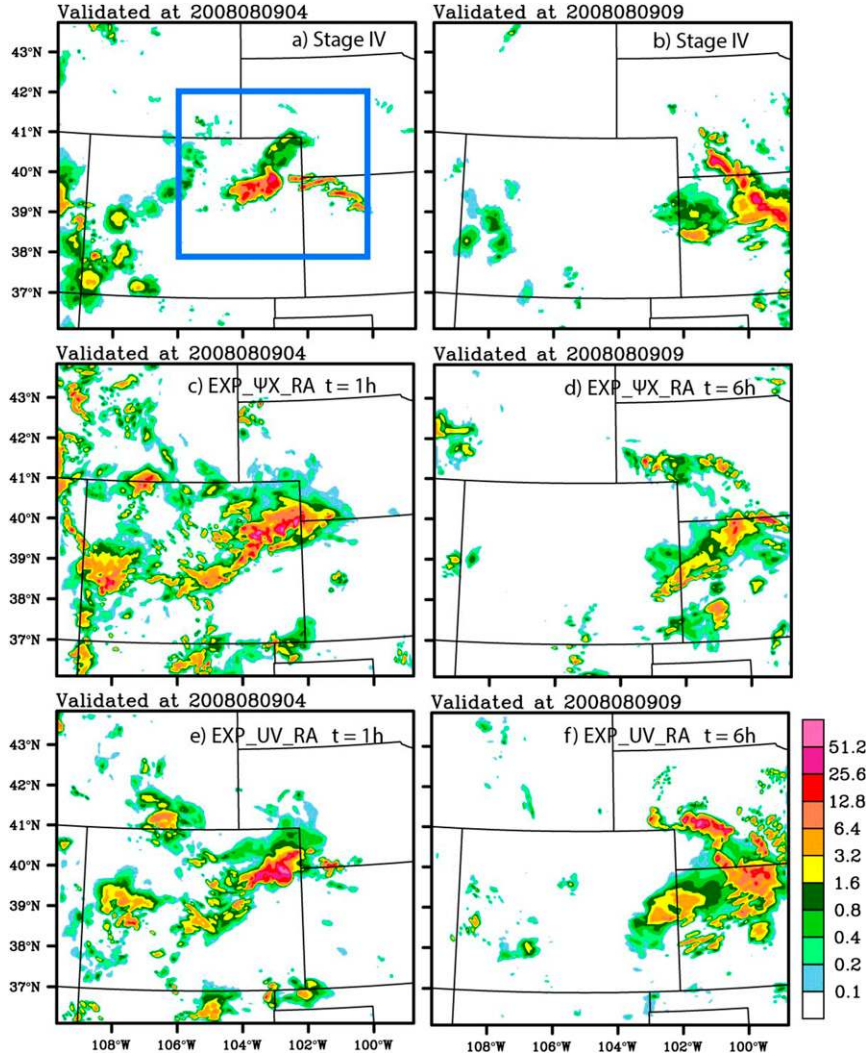
FIG. 14. Forecasts of 1-h accumulated precipitation at $t = 1$ h for (c) EXP_$\psi\chi$_RA0.5 and (e) EXP_UV_RA0.5, and at $t = 6$ h for (d) EXP_$\psi\chi$_RA0.5 and (f) EXP_UV_RA0.5. (a),(b) The stage-IV precipitation analyses at these two forecast times are displayed, respectively, for verification. The blue rectangle in (a) is the subdomain used for Fig. 16.

of the major precipitation system and the number of false alarm cells. The development of the secondary convective band in Kansas and Nebraska is forecasted quite well by the experiment EXP_UV_RA (Fig. 16f), but not by EXP_$\psi\chi$_RA (Fig. 14e).

To gain an understanding about what caused the differences in the precipitation forecasts, the increments of u, T, and RH from the experiments EXP_UV_RA and EXP_$\psi\chi$_RA at 0300 UTC are examined and compared in Fig. 15. Both the increments of u and T clearly show larger-scale patterns for the experiment CV_$\psi\chi$_RA in comparison with CV_UV_RA. The increments of u from EXP_UV_RA mainly concentrate in Colorado and Wyoming where the convective activities occur while the

increments are much smaller in other parts of the domain. This increment pattern is desirable because it is expected that the convective-scale DA adds disturbances in the convective region while maintaining the existing large-scale balance in the surrounding environment from the first guess. In contrast to EXP_UV_RA, there are large increments from EXP_$\psi\chi$_RA over the east and southeast parts of the domain, which is not desirable and lacks physical explanations. The relative humidity shows a strip of moistening in northeastern Colorado from EXP_UV_RA, where the major precipitation system occurs, in comparison with EXP_$\psi\chi$_RA.

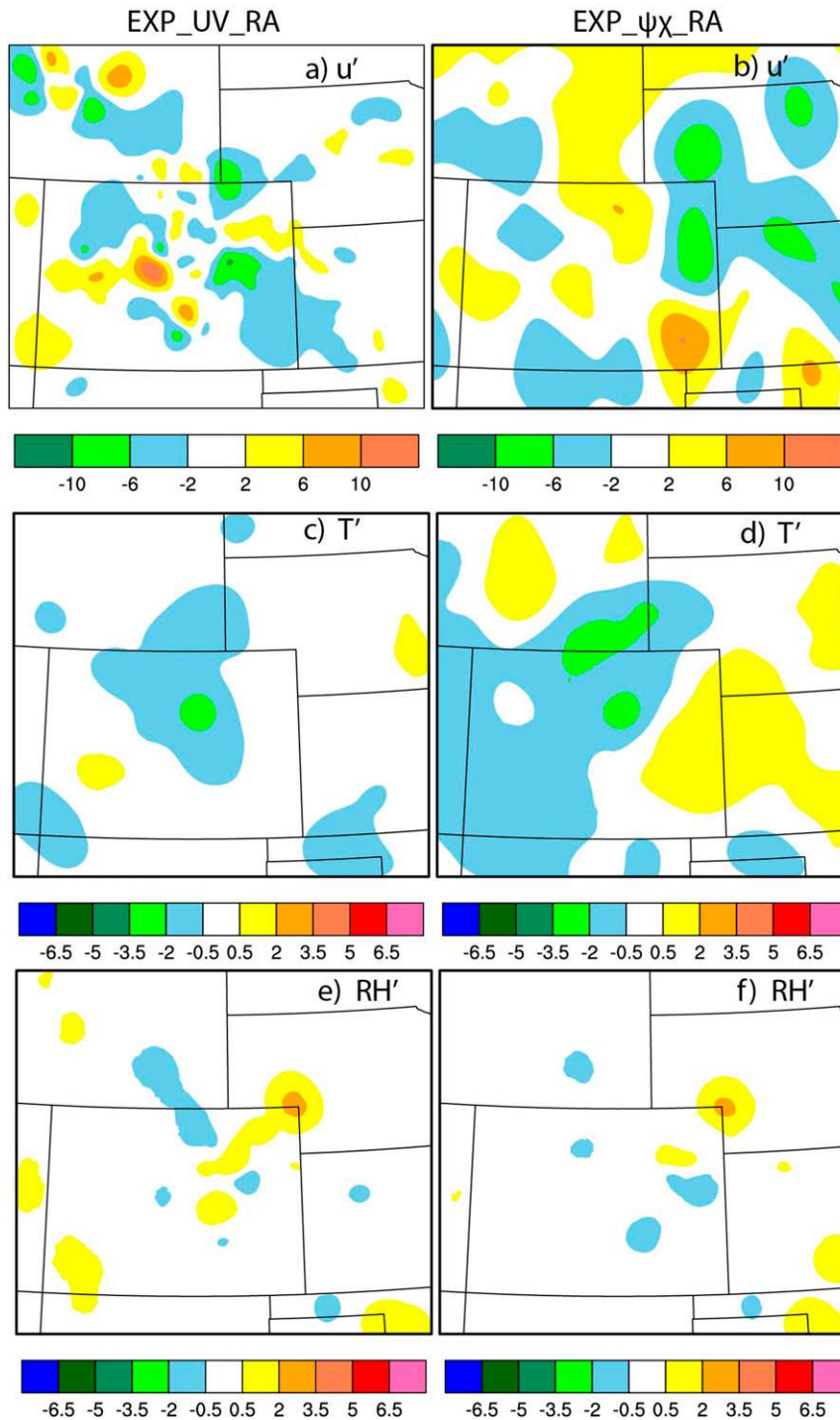The vertical motion fields from both experiments (Fig. 16) show areas of strong updrafts in northeastern

FIG. 15. Analysis increments of (a),(b) *u*; (c),(d) *T*; and (e),(f) RH at the fifth model level (~265 m). (left) EXP_UV_RA0.5 and (right) EXP_$\psi\chi$_RA0.5.

Colorado; however, the details of the updraft structures are noticeably different. Note that in Fig. 16 we show the vertical velocity and horizontal wind vector fields of the two experiments at *t* = 1 h rather than at the analysis

time because the vertical velocity is not an analysis variable in WRF 3DVar. The gust front (marked by "GF" in Fig. 16b) is revealed in EXP_UV_RA by the strong vertical velocity associated with the convergence
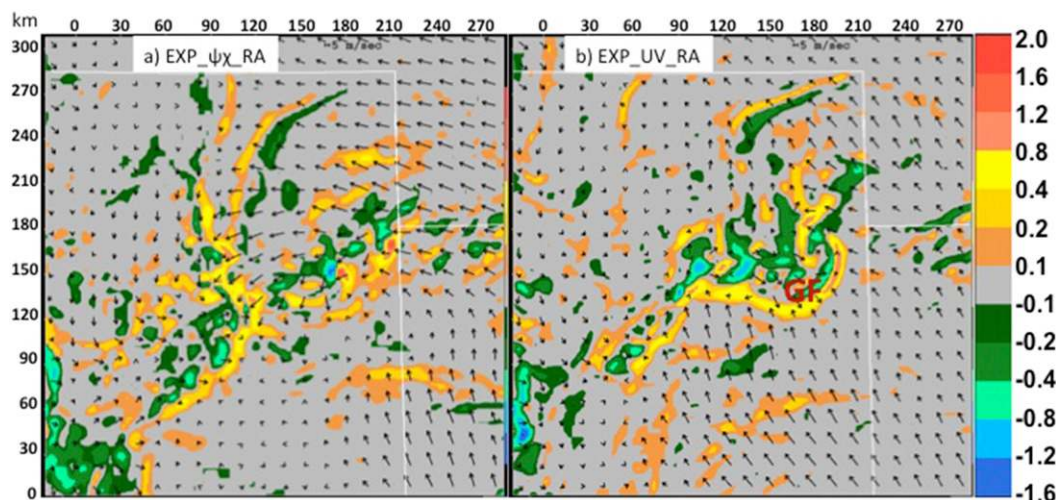
FIG. 16. Vertical velocity fields overlaid by horizontal wind vectors on the level of 150 m above ground at $t = 1$ h from (a) EXP_$\psi\chi$_RA0.5 and (b) EXP _UV_RA0.5. Note that the plots are on a subdomain of the 3-km experimental domain indicated in Fig. 14a.

between the prestorm environmental southeasterly flow and the northwesterly outflow from the storm. In Fig. 16a, the southeasterly flow is clearly disturbed; consequently, the main convergence zone is moved to the west of the GF shown in Fig. 16b and has a north–south orientation, resulting in a larger precipitation band (see Fig. 14c).

Using the radial velocity observations from the radars in the domain, we verified the accuracy of the 12-h wind forecasts from the two no-radar experiments and the two radar experiments. The results are given in Fig. 17. The verification confirms that CV_UV produces more accurate wind forecasts with and without radar DA due to the improved initial wind analysis. The wind forecast from EXP_UV is improved over that from EXP_$\psi\chi$ for the entire 12-h forecast period. The wind forecast using CV_UV is further improved when radar observations are assimilated. In contrast, the wind forecast using CV_$\psi\chi$ is degraded after $t = 8$ h from its counterpart without radar data, which could be the reason for the degraded precipitation forecast at later hours when radar data are assimilated. The fact that the skills of both the precipitation and wind forecasts persist for the entire 12-h forecast range is an indication that physically meaningful small-scale features have been added to the analysis by the closer fitting to the radial wind in CV_UV.

In summary, the experiments in this section suggest that the $\psi\chi$-based 3DVar has difficulties in fitting analyses to the high-resolution observations. The degree of fitting can be improved when the length scales are reduced, however, the positive impact on the precipitation forecast lasts only for a few hours for the experiment using CV_$\psi\chi$. Although most previous studies using

WRF 3DVar and CV_$\psi\chi$ have shown that radar DA can have a positive impact on short-term precipitation forecasts, it is not unusual for any positive impact to disappear after a few hours. For example, Sun et al. (2012) found from statistical results obtained over a period of active convective days that positive impacts lasted for 6–8 h. Although there could be several reasons for the short-term positive impact, our current study suggests that the proper selection of momentum control variables has the potential to extend the period during which the radar observations produce a positive impact on precipitation prediction.

6. Summary and conclusions

In this study, we compared the background error characteristics of two momentum control variable
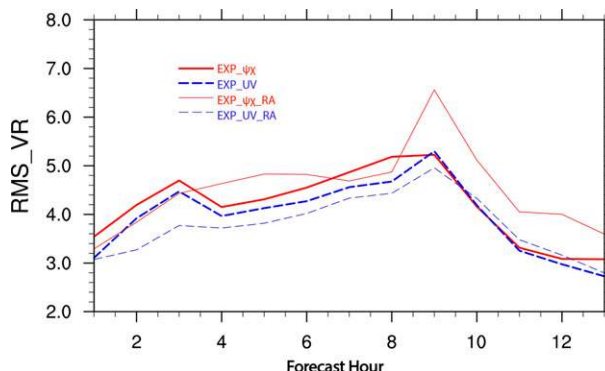

FIG. 17. Root-mean-square error of forecast radial velocity verified against observations from six Doppler radars in the analysis domain.

options for variational data assimilation and their impacts on short-term convective forecasting. The error statistics are derived from a forecast difference ensemble generated by the 3-km WRF real-time forecasts during May and June 2012 over a domain in the United States using the NMC method. By comparing the error statistics of $\psi\chi$ and UV, we have found that the correlation between u and v is small and notably smaller than that between ψ and χ, which provides the justification that u and v can be treated as independent control variables. We have shown that the additional step of variable transformation between $\psi\chi$ and UV in CV_$\psi\chi$ results in larger length scale and smaller variance, in spectral space, of u and v from the BE modeling. We have also found that the spatial correlation of velocity is negative at long distances and that the problem is amplified when the length scale is tuned to a smaller value. The larger length scale and smaller variance from CV_$\psi\chi$ produce analysis increments that tend to miss small-scale features.

Both control variable options were applied to seven historical convective cases that occurred in the Rocky Mountain Front Range region. Precipitation skill scores over 29 short-term forecasts showed that the experiment using CV_UV produced improved skills especially at the later hours of 0–12-h forecasts. The experiments using CV_UV enable the organization of the convective systems and show improved skill for the organized systems.

The case of 9 August 2008 was examined in more detail by adding the assimilation of eight NEXRADs in the 3-km inner domain. It was found that CV_UV enables a 3DVar analysis that fits closer to the radial velocity observations and the analysis using CV_UV improves the precipitation forecast skill with or without radar data over that using CV_$\psi\chi$. It was also shown that the use of different momentum control variables in the 3DVar system results in notable discrepancies in the horizontal wind and vertical velocity, causing forecast discrepancies in precipitation. The wind increment from CV_UV showed small-scale disturbances where the convective activities occur while maintaining the background large-scale balance in the surrounding environment. In contrast to EXP_UV_RA, the increment pattern from EXP_$\psi\chi$_RA is more widespread, which may have contributed to the degraded forecast with respect to its counterpart experiment without radar. CV_UV enables an improved forecast of the vertical velocity field associated with the convergence between the prestorm environmental southeasterly flow and the northwesterly outflow from the storm. The wind forecasts from the experiment using CV_UV are more accurate as verified by the radar radial velocity observations.

Another choice of the momentum control variables that is not compared in the current study is vorticity and divergence. Xie and MacDonald (2012) showed that a vorticity/divergence-based 3DVar was comparable with the UV-based 3DVar in terms of producing accurate velocity analysis. However, they pointed out that the implementation of the vorticity and divergence 3DVar is more complex and numerically inefficient because it requires solving the Poisson equations for every minimization iteration. It would nevertheless be of interest to compare the BE characteristics and performance of the UV 3DVar with that of a vorticity/divergence 3DVar in the context of high-resolution analysis and forecast.

REFERENCES

Barker, D. M., W. Huang, Y.-R. Guo, A. J. Bourgeois, and Q. N. Xiao, 2004: A three-dimensional variational data assimilation system for MM5: Implementation and initial results. *Mon. Wea. Rev.*, **132**, 897–914, doi:10.1175/1520-0493(2004)132<0897:ATVDAS>2.0.CO;2.

——, and Coauthors, 2012: The Weather Research and Forecasting Model's Community Variational/Ensemble Data Assimilation System: WRFDA. *Bull. Amer. Meteor. Soc.*, **93**, 831–843, doi:10.1175/BAMS-D-11-00167.1.

Berre, L., 2000: Estimation of synoptic and mesoscale forecast error covariances in a limited-area model. *Mon. Wea. Rev.*, **128**, 644–667, doi:10.1175/1520-0493(2000)128<0644:EOSAMF>2.0.CO;2.

Courtier, P., J.-N. Thépaut, and A. Hollingsworth, 1994: A strategy for operational implementation of 4D-Var, using an incremental approach. *Quart. J. Roy. Meteor. Soc.*, **120**, 1367–1387, doi:10.1002/qj.49712051912.

Derber, J., and F. Bouttier, 1999: A reformulation of the background error covariance in the ECMWF global data assimilation system. *Tellus*, **51A**, 195–221, doi:10.1034/j.1600-0870.1999.t01-2-00003.x.

Errico, R. M., N. C. Privé, and W. Gu, 2015: Use of an OSSE to evaluate background-error covariances estimated by the NMC method. *Quart. J. Roy. Meteor. Soc.*, **141**, 611–618, doi:10.1002/qj.2384.

Gao, J., M. Xue, A. Shapiro, and K. K. Droegemeier, 1999: A variational analysis for the retrieval of three-dimensional mesoscale wind fields from two Doppler radars. *Mon. Wea. Rev.*, **127**, 2128–2142, doi:10.1175/1520-0493(1999)127<2128:AVMFTA>2.0.CO;2.

Ge, G., J. Gao, and M. Xue, 2012: Diagnostic pressure equation as a weak constraint in a storm-scale three-dimensional variational radar data assimilation system. *J. Atmos. Oceanic Technol.*, **29**, 1075–1092, doi:10.1175/JTECH-D-11-00201.1.

Hayden, C. M., and R. J. Purser, 1995: Recursive filter objective analysis of meteorological fields: Applications to NESDIS operational processing. *J. Appl. Meteor.*, **34**, 3–15, doi:10.1175/1520-0450-34.1.3.

Huang, X.-Y., and Coauthors, 2009: Four-dimensional variational data assimilation for WRF: Formulation and preliminary results. *Mon. Wea. Rev.*, **137**, 299–314, doi:10.1175/2008MWR2577.1.

Ingleby, N., 2001: The statistical structure of forecast errors and its representation in The Met. Office global 3-D variational data assimilation scheme. *Quart. J. Roy. Meteor. Soc.*, **127**, 209–231, doi:10.1002/qj.49712757112.

Lin, Y., and K. E. Mitchell, 2005: The NCEP Stage II/IV hourly precipitation analyses: Development and applications. *19th Conf. on Hydrology*, San Diego, CA, Amer. Meteor. Soc., 1.2. [Available online at https://ams.confex.com/ams/Annual2005/techprogram/paper_83847.htm.]

Lorenc, A. C., 1986: Analysis method for numerical weather prediction. *Quart. J. Roy. Meteor. Soc.*, **112**, 1177–1194, doi:10.1002/qj.49711247414.

——, and Coauthors, 2000: The Met. Office global three-dimensional variational data assimilation scheme. *Quart. J. Roy. Meteor. Soc.*, **126**, 2991–3012, doi:10.1002/qj.49712657002.

Parrish, D., and J. Derber, 1992: The National Meteorological Center's spectral statistical interpolation analysis system. *Mon. Wea. Rev.*, **120**, 1747–1763, doi:10.1175/1520-0493(1992)120<1747:TNMCSS>2.0.CO;2.

Rawlins, F., S. P. Ballard, K. J. Bovis, A. M. Clayton, D. Li, G. W. Inverarity, A. C. Lorenc, and T. J. Payne, 2007: The Met Office global four-dimensional variational data assimilation scheme. *Quart. J. Roy. Meteor. Soc.*, **133**, 347–362, doi:10.1002/qj.32.

Skamarock, W. C., and Coauthors, 2008: A description of the Advanced Research WRF version 3. NCAR Tech. Note NCAR/TN-475+STR, 113 pp. [Available online at http://www.mmm.ucar.edu/wrf/users/docs/arw_v3_bw.pdf.]

Sun, J., and N. A. Crook, 1997: Dynamical and microphysical retrieval from Doppler radar observations using a cloud model and its adjoint. Part I: Model development and simulated data experiments. *J. Atmos. Sci.*, **54**, 1642–1661, doi:10.1175/1520-0469(1997)054<1642:DAMRFD>2.0.CO;2.

——, D. W. Flicker, and D. K. Lilly, 1991: Recovery of three-dimensional wind and temperature fields from single-Doppler radar data. *J. Atmos. Sci.*, **48**, 876–890, doi:10.1175/1520-0469(1991)048<0876:ROTDWA>2.0.CO;2.

——, S. B. Trier, Q. Xiao, M. L. Weisman, H. Wang, Z. Ying, M. Xu, and Y. Zhang, 2012: Sensitivity of 0–12-h warm-season precipitation forecasts over the central United States to model initialization. *Wea. Forecasting*, **27**, 832–855, doi:10.1175/WAF-D-11-00075.1.

Wang, H., J. Sun, S. Fan, and X.-Y. Huang, 2013a: Indirect assimilation of radar reflectivity with WRF 3D-Var and its impact on prediction of four summertime convective events. *J. Appl. Meteor. Climatol.*, **52**, 889–902, doi:10.1175/JAMC-D-12-0120.1.

——, ——, X. Zhang, X.-Y. Huang, and T. Auligné, 2013b: Radar data assimilation with WRF 4D-Var. Part I: System development and preliminary testing. *Mon. Wea. Rev.*, **141**, 2224–2244, doi:10.1175/MWR-D-12-00168.1.

——, X. Huang, J. Sun, D. Xu, M. Zhang, S. Fan, and J. Zhong, 2014: Inhomogeneous background error modeling for WRF-Var using the NMC method. *J. Appl. Meteor. Climatol.*, **53**, 2287–2309, doi:10.1175/JAMC-D-13-0281.1.

Wu, W., and J. Purser, 2002: Three-dimensional variational analysis with spatially inhomogeneous covariances. *Mon. Wea. Rev.*, **130**, 2905–2916, doi:10.1175/1520-0493(2002)130<2905:TDVAWS>2.0.CO;2.

Xiao, Q., Y.-H. Kuo, J. Sun, W.-C. Lee, E. Lim, Y. Guo, and D. M. Barker, 2005: Assimilation of Doppler radar observations with a regional 3D-Var system: Impact of Doppler velocities on forecasts of a heavy rainfall case. *J. Appl. Meteor.*, **44**, 768–788, doi:10.1175/JAM2248.1.

Xie, Y., and A. E. MacDonald, 2012: Selection of momentum variables for a three-dimensional variational analysis. *Pure Appl. Geophys.*, **169**, 335–351, doi:10.1007/s00024-011-0374-3.

——, C. Lu, and G. L. Browning, 2002: Impact of formulation of cost function and constraints on three-dimensional variational data assimilation. *Mon. Wea. Rev.*, **130**, 2433–2447, doi:10.1175/1520-0493(2002)130<2433:IOFOCF>2.0.CO;2.

Zou, X., Y.-H. Kuo, and Y.-R. Guo, 1995: Assimilation of atmospheric radio refractivity using a nonhydrostatic adjoint model. *Mon. Wea. Rev.*, **123**, 2229–2249, doi:10.1175/1520-0493(1995)123<2229:AOARRU>2.0.CO;2.

Zupanski, M., D. Zupanski, T. Vukicevic, K. Eis, and T. Vonder Haar, 2005: CIRA/CSU four-dimensional variational data assimilation system. *Mon. Wea. Rev.*, **133**, 829–843, doi:10.1175/MWR2891.1.